# Elastic interaction-induced anisotropic growth of dislocation loop arrays

**Pranay Chakraborty[1], Tengfei Ma[1], Yinan Cui[2,a], Abigail Hunter[3,a], Lei Cao[1,a]** (iD)

[1] *Department of Mechanical Engineering, University of Nevada, Reno, NV 89557, USA*
[2] *Department of Engineering Mechanics, Tsinghua University, Beijing 100084, China*
[3] *X Computational Physics Division, Los Alamos National Laboratory, Los Alamos, NM 87545, USA*
[a] Address all correspondence to these authors. e-mails: cyn@mail.tsinghua.edu.cn; ahunter@lanl.gov; leicao@unr.edu

The elastic interactions and reactions of dislocations lead to the formation of complex dislocation substructures, which is critical to the strain hardening and fatigue failure. Phase field dislocation dynamics simulations are conducted as a first step to understand the elastic interactions between dislocation loops. When the interloop spacing is small, the elastic interactions with neighboring loops become strong, rendering the edge segments strongly pinned, while allowing for the screw segments to propagate more easily. The interactions are found to result in an anisotropic stress distribution around the dislocation loops, leading to the formation of arrays of long, straight edge dislocations that could act as barriers to subsequent slip. Furthermore, the effect of initial loop size and applied strain rate on the elastic interaction-induced anisotropic pinning effect is investigated and discussed. The results are important for coarse-graining dislocation substructures formation into continuum level models of deformation in crystalline solids.

## Introduction

Plasticity determines the strength and ductility of structural metals and alloys. Macroscopic plasticity is, microscopically, mediated by the evolution of crystalline defects, among which dislocations play a key role. In response to mechanical loading, the density of dislocations increases rapidly as a result of the growth of existing dislocations and the nucleation of new dislocations. In a structure with high dislocation density, dislocations often form complex patterns and substructures, such as walls [1, 2], cells [3], labyrinth structures [4], and dislocation subgrain boundaries [5], under both monotonic and cyclic loading [4–6]. The impact of these dislocation substructures on further plastic deformation is twofold: they can exert a back stress and thus increase the activation stress and eventually halt dislocation nucleation from Frank-Read sources; they can also directly impede the gliding of other dislocations. As a result, the strength of metals is known to increase with the density of dislocations, which is embodied by the classical Taylor's equation [7]. On the other hand, dislocation substructures such as the persistent slip bands naturally appear under cycling loading, and they are precursor to fatigue failure [4, 6]. Despite its importance

in the stress–strain response [8–10] and fatigue failure [4, 6], our understanding of the formation mechanism of the dislocation substructures is still very limited [11–14].

Previous experimental studies focused on the effect of loading conditions, grain orientations, and correlating the formation of dislocation substructures to stress–strain curves [15, 16]. Meanwhile, many computational efforts using both micro/mesoscopic and continuum level models successfully simulated the dislocation substructure formation [13, 17–24]. In particular, dislocation cross slip was found to be a necessary condition for the formation of dislocation substructures by both discrete dislocation dynamics [25–27] and dislocation density based simulations [28]. In contrast, in the absence of cross slip, dislocation patterning was predicted in single slip simulations adopting discrete dislocation dynamics simulations [29] and continuum dislocation plasticity simulations [30], highlighting the importance of long-range elastic interactions between dislocations. The objective of this work is to study the elastic interactions of curved dislocations using 3D phase field dislocation dynamics (PFDD) simulations. We simulate the growth of an array of dislocation loops, which have been reported in fatigued material [31] and irradiated materials [32], on parallel planes and find

that the elastic interaction between the loops results in pinning of the edge segments. Understanding the origin and evolution of such dislocation interactions is important for coarse-graining the effects of dislocation substructures into continuum level models of deformation in crystalline solids [30, 33]. Particularly, we aim to gain an in-depth understanding of the interactions between the stress fields that cause the formation of the dislocation wall structures that is critical for straining hardening and ductility of materials. Though it is known that the elastic interactions between dislocations generally increases as the interloop spacing decreases, no one has reported how, quantitatively, the interactions impact the morphology of growing loops.

PFDD tracks the evolution of phase field variables, of which an integer jump represents the location of an individual dislocation. A unique feature of the PFDD model is that it is energy-based, such that the evolution of dislocations (i.e., the phase field variables) is driven by the minimization of the total system energy [34]. This allows PFDD to naturally incorporate information such as the material $\gamma$-surface, which is the energy required as atoms shift due to translations along a slip plane [35, 36]. This is particularly advantageous for modeling partial dislocations and stacking faults, which critically influence the plasticity of nanostructured metals. Consequently, PFDD has been applied to model many aspects of plasticity in face-centered cubic (fcc) nanocrystalline metals and thin films [37, 38]. For example, Hunter et al. used PFDD simulations to construct the relationship between the unstable stacking fault energy, shear modulus, and the equilibrium stacking fault width among various fcc metals [39]. Adopting the similar approach, Cao et al. studied the effect of grain size [40] and strain rate [41] on the competition between partial dislocations and full dislocations in nanostructured fcc metals. Furthermore, significant progress has been made in modeling the interactions between dislocations and grain boundaries using the PFDD model. Grain boundaries can be modeled as regions with a high density of sessile dislocations, and thus the interaction between grain boundaries and lattice dislocations are mediated by the elastic interaction and dislocation reaction among them [40]. In particular, Cao et al. demonstrated the nucleation of dislocation loops from grain boundary regions and the subsequent transmission of the loop into neighboring grains, which is in good agreement with atomistic simulations [40]. Besides polycrystals, Hunter et al. have successfully predicted the transmission of lattice dislocations across the bi-metal interfaces [42]. More recently, PFDD model has been extended to other material systems, such as body-centered cubic metals [43–45], high entropy alloys [46], and hexagonal closed packed metals [47]. Finally, we emphasize that PFDD has the advantage over other dislocation dynamics methods in that it naturally handles the dissociated core structure and interaction with grain boundaries and precipitates, thus allowing us to explore dislocation patterning in regimes that are not accessible

to other methods. One particular scenario where PFDD excels is to model the formation of dislocation substructure considering precipitates. Therefore, the PFDD method has the potential to inform the design of material microstructure toward favorable mechanical properties.

This paper is organized as follows: In "Results and discussion" section, we present the effect of the interloop spacing, initial loop size, and strain rate on the elastic interactions between dislocation loops and the corresponding pinning of the edge segments, as obtained from the PFDD simulations. We conclude this paper in "Conclusions" section. The formulation of the PFDD model and the setup of our simulations are detailed in "Methods" section.

## Results and discussion

### The effect of the interloop spacing

First, we simulate the growth of dislocation loops that have an initial radius of $r = 5b$ and an interloop spacing ($d$) that varies from 4 to 64$b$. In Fig. 1, we take a cross-section of the simulation cell, looking down along the slip plane normal onto one active slip plane and plot the phase field variable ($\xi$), in which the jump in $\xi$ represents the location of the dislocation line.

For the largest interloop spacing of $d = 64b$ (Fig. 1a), both the screw and edge segments of the dislocation loop grow significantly in response to the applied strain. As the interloop spacing decreases (Fig. 1b–e), we observe distinctively different loop shapes as the loops expand. In particular, for the smallest interloop spacing of $d = 4b$, the screw segments propagate $\sim 60b$ and reach the boundary of the simulation domain, while the edge segments only propagate $\sim 7b$, when the applied strain reaches 0.088. The fast propagation of the screw segment continues to deposit new dislocation segments of edge-type, leading to the formation of a lens-shaped dislocation loop with extremely long edge segments (Fig. 1e).

It is known that dislocations with edge and screw characters in fcc materials have similar mobility. Therefore, the initially circular dislocation loop is expected to maintain a circular shape as it expands over time without the impedance of other defects, such as obstacles, junctions, or free surfaces. This can indeed be seen from the case of $d = 64b$ (Fig. 1a). The initially circular loop evolves to have a slight oval shape, in which the slightly longer screw segment than edge segment is due to the lower self-energy of the former than the latter [48]. We have also simulated larger interloop spacing ($d \geq 64b$), and no difference was seen in the loop morphology in comparison to the case of $d = 64b$. Hence, we can assume that the long-range elastic interaction between dislocation loops on different slip planes is weak when the interloop spacing is larger than 64$b$, and the case of $d = 64b$ is representative of a single isolated dislocation loop. We also note
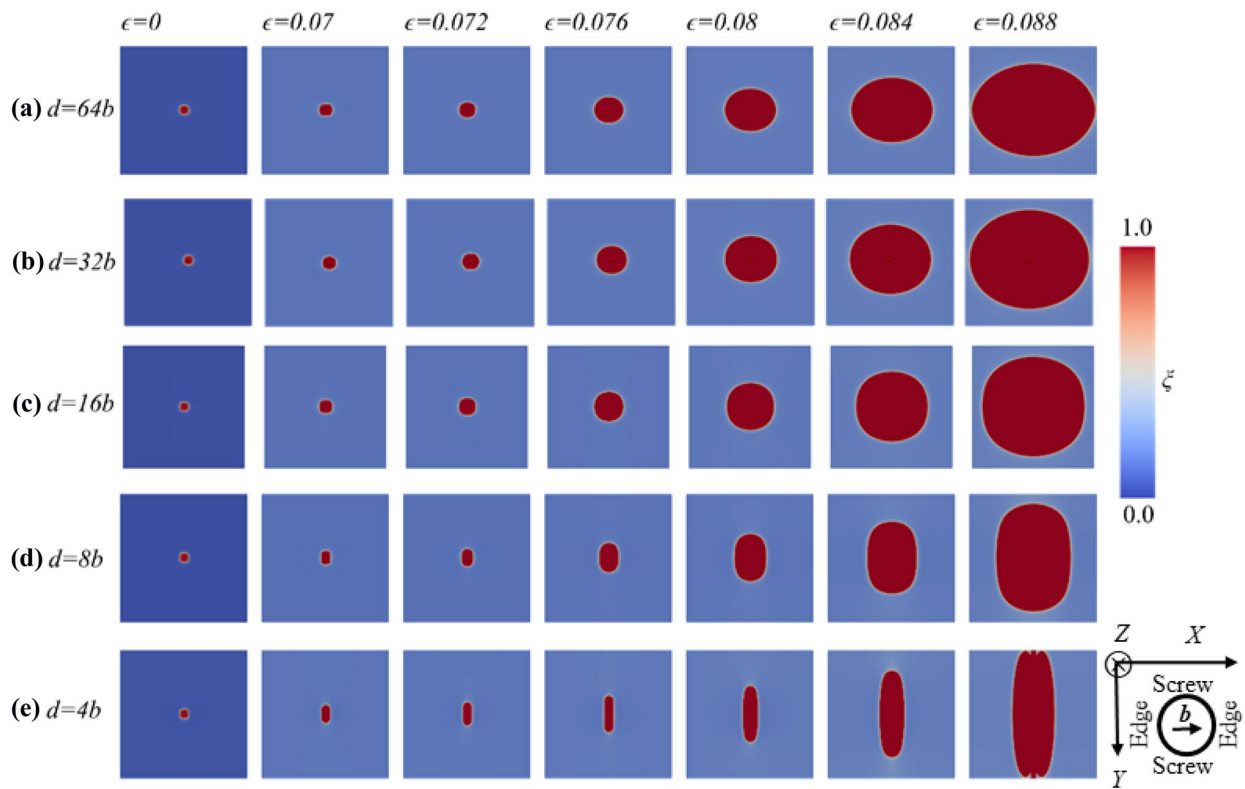
**Figure 1:** Growth of one dislocation loop within an array under increasing applied strain. The dislocation loop has an initial radius of $r = 5b$. The interloop spacing $d$ varies between 4 and $64b$, significantly affecting the morphology of the dislocation loop as it expands. The loop lies on the $X$–$Y$ plane, and the segment of the dislocation loop that is perpendicular (parallel) to the vector $b$ represents the pure edge (pure screw) segment. Schematics of the pure edge (and pure screw) segments of a dislocation loop and Burger's vector with reference to the coordinate system are provided on the lower right corner of the panel.

that the oval shape becomes a bit more pronounced as the loop approaches the simulation cell boundaries and begins to interact (attract) with its periodic images. On the other hand, the lens-shaped loop for smaller interloop spacing is surprising, especially as the applied loading is homogeneous. Only observed for small interloop spacing ($d = 4b$ and $8b$), the lens shape may be caused by the occurrence of strong elastic interactions between dislocation loops positioned close together. To study the elastic interactions between loops, we examine the local stress field

around the dislocation loop at zero applied loading. Based on the Peach–Koehler equation, the shear stress $\tau = \sigma_{zx}$ provides the driving force for loop growth, and its contour plot for different interloop spacings is shown in Fig. 2.

As discussed previously, the case of $d = 64b$ can be considered representative of a single isolated dislocation loop [49]. As expected, the stress field in this case decays moving away from the dislocation line (Fig. 2a). For $d = 32b$ (Fig. 2b), the stress distribution is very similar to that seen in the $d = 64b$
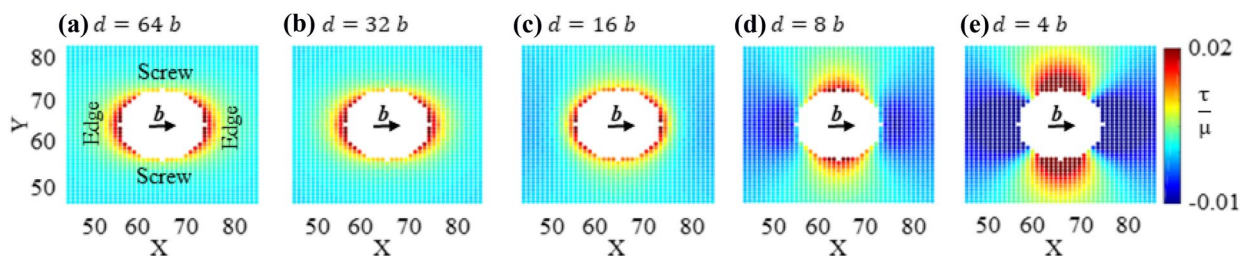


**Figure 2:** Contour plot of the normalized shear stress $\tau = \sigma_{zx}$ around the dislocation loop with $r = 5\,b$ at zero strain predicted by the PFDD simulations. The stress inside the loop is removed for clarity. In a pure edge (perpendicular to Burger's vector $b$) and pure screw (parallel to $b$) segments of the dislocation loop are shown.

case. As such, for larger interloop spacing ($d = 32b$ or $64b$), the stress distribution and thus, the loop morphology (Fig. 1a and b) are close to the case of a single, isolated dislocation loop. As the interloop spacing becomes smaller and the elastic interaction becomes stronger, the stress distribution around the loop becomes distinctively different from the previous cases. Specifically, for $d = 8b$ and $4b$ (Fig. 2d, e), the stress distribution shows a highly anisotropic pattern: positive $\tau$ near the screw-type loop segments and negative $\tau$ near the edge-type loop segments. According to the Peach-Koehler equation, the loop will expand when $\tau > 0$ and collapse when $\tau < 0$. Therefore, at zero applied loading, the edge segment is under a stress state in favor of loop collapse, while the screw segment is under a stress state in favor of loop growth, for $d = 8b$ and $4b$.

After unveiling the elastic interaction-induced anisotropic stress distribution around the dislocation loop, we can now explain the anisotropic loop expansion presented in Fig. 1d and e. Upon the application of homogeneous loading, the edge segment first remains sessile until the applied loading overcomes the elastic interaction-induced negative stress fields near the edge segments. In contrast, the screw segment begins to glide earlier, which is assisted by the elastic interaction-induced positive stress near the screw segment. Thus, the Peach-Koehler force at the screw-type portions of the loop is always much larger than at edge-type segments. As a result, the screw segment propagates much faster than the edge segment, resulting in elongated edge segments. In other words, the elastic interaction between loops on different slip planes becomes stronger with decreasing interloop spacing, resulting in local stress fields that significantly differ from the applied loading and strongly "pin" the edge segments.

Next, we will examine the elastic interaction-induced shear stress in a loop array analytically to validate our observation of the pinning effect. While the stress fields surrounding straight dislocation lines are well known, that for a curved dislocation loop is complicated and the explicit form was only derived recently [50]. Equation (1) shows the analytical shear stress exerted by a dislocation loop,
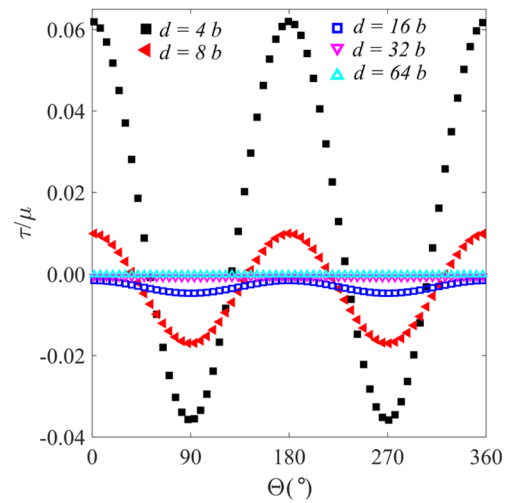


**Figure 3:** Distribution of the shear stress $\tau_{inter}$ around the dislocation loop at zero applied strain calculated with the superposed analytical solution describing the stress caused by elastic interactions between loops.

loop in the cylindrical coordinates. First, the shear stress caused by each dislocation loop in the array is calculated using Eq. (1). Then, the superposition of these stresses equals the elastic interaction-induced shear stress in a loop array. Specifically, the number of loops in the array was chosen to be 10 because the stress profile does not change if we include more loops.

The calculated interaction stress, $\tau_{inter}$ around one dislocation loop within the array is shown in Fig. 3. The shear stress is shown for various interloop spacings as a function of the angle ($\theta$) between the Burgers vector and the dislocation line sense, i.e., $\theta = 0°$, 180° for screw character and $\theta = 90°$, 270° for edge character. Notably, the anisotropic stress pattern predicted by the PFDD simulations (see contours in Fig. 2) is also observed in the analytical stress field: $\tau_{inter}$ becomes negative at the edge segments and positive at the screw segments for $d = 4b$ and $8b$. Furthermore, Fig. 3 clearly demonstrates that the elastic interactions are strong for $d = 4b$ and $8b$, but become weaker for $d \geq 16b$, validating the elastic interaction-induced pinning of the edge segments observed in our PFDD simulations.

$$\sigma_{zx} = \left( b\mu \left( -EllipticK\left[ -\frac{4rr_o}{z^2 + (r - r_o)^2} \right] (z^2 + (r + r_o)^2) \left( r^2 (z^4 - r^4(-2 + v) - z^4 v + 5z^2 r_o^2 - 2z^2 v r_o^2 + 2r_o^4 - v r_o^4 + r^2(3z^2 - 2z^2 v - 4r_o^2 + 2v r_o^2)) \right. \right. \right.$$

$$+ \cos[2\theta] \left( r^6 v + r^4 z^2(3 + 4v) + 2(z^2 + r_o^2)^2(z^2 + z^2 v + v r_o^2) + r^2(5z^4 + 5z^4 v - 5z^2 r_o^2 + 2z^2 v r_o^2 - 3v r_o^4) \right) + EllipticE\left[ -\frac{4rr_o}{z^2 + (r - r_o)^2} \right] \left( r^2(-r^6(-2 + v) \right.$$

$$+ r^4(5z^2 - 3z^2 v - 6r_o^2 + 3v r_o^2) + r^2(4z^4 - 3z^4 v - 10z^2 r_o^2 + 2z^2 v r_o^2 + 6r_o^4 - 3v r_o^4) + (z^2 + r_o^2)(z^4 - z^4 v + 7z^2 r_o^2 - 2r_o^4 + v r_o^4))$$

$$+ \cos[2\theta] \left( r^8 v + r^6(3z^4 + 5z^2 v - 5v r_o^2) + 2(z^2 + r_o^2)^3(z^2 + z^2 v + v r_o^2) - r^2(z^2 + r_o^2)(-7z^4 - 7z^4 v + 9z^2 r_o^2 + 7v r_o^4) + r^4(8z^4 + 9z^4 v + 4z^2 r_o^2 - 6z^2 v r_o^2 + 9v r_o^4)) \right) \right) / $$

$$(4\pi r^2(-1 + v)(z^2 + (r - r_o)^2)^{3/2}(z^2 + (r + r_o)^2)^2),$$

$$(1)$$

where $v$ is Poisson's ratio and $\mu$ is the shear modulus, $r_0$ is the radius of the dislocation loop. $r$, $\theta$ and $z$ represent the position of the reference point with respect to the center of the dislocation

### The effect of the dislocation loop size

So far, we have demonstrated that the elastic interaction-induced pinning effect results in long edge segments for interloop
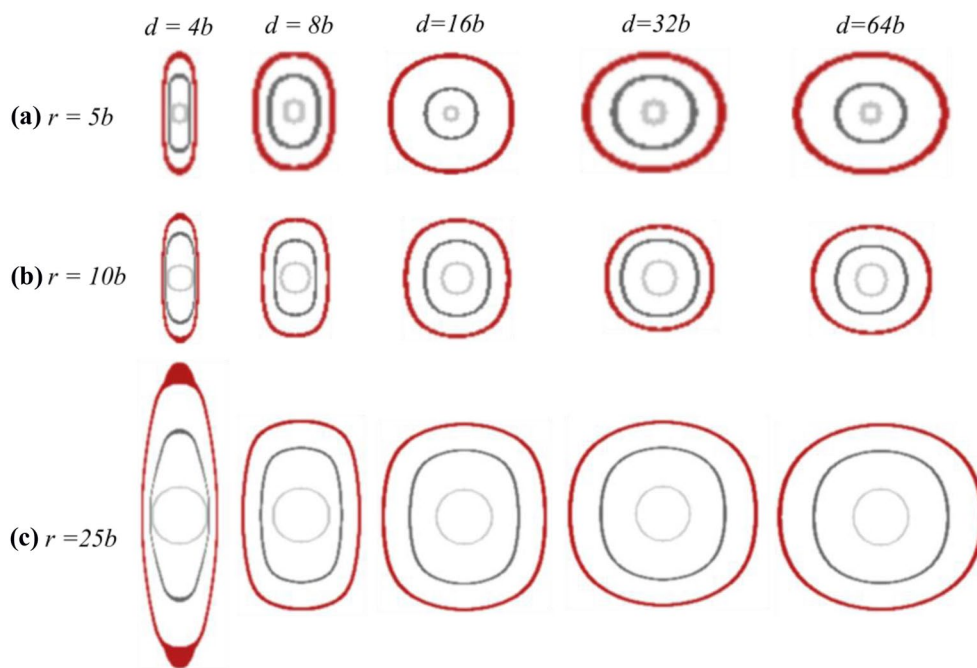
**Figure 4:** Growth of a dislocation loop within an array where the initial dislocation loop has a radius of (a) $r = 5b$, (b) $10b$, or (c) $25b$. The interloop spacing $d$ varies between 64 and $4b$. Light gray, gray, and red colored loops represent the loop configurations at the initial (at $\epsilon = 0$), intermediate (at $\epsilon \approx 0.038$), and final (at $\epsilon = 0.076$) strain, respectively.

spacings of $d = 4b$ or $8b$, which is roughly smaller than the initial loop size ($2r = 10b$). In this section, we investigate the effect of the initial loop size as realistic dislocation loops can be orders of magnitude larger than the case considered previously ($r = 5b$). As such, we compare the growth of loop arrays with initial radii of $r = 5b$, $10b$, and $25b$ and demonstrate the evolution of one dislocation loop within the array in Fig. 4, in which different colors indicate increasing applied strains. As expected, for smaller interloop spacings (i.e., $d = 4b$ and $8b$), we observe the pinning effect on the edge segment for all three loop sizes. With further examination of the interloop spacing $d = 16b$, we find that loops with the initial size of $r = 25b$ or $10b$ also have longer edge segments than screw segments (Fig. 4b, c), while the loops with the initial size of $r = 5b$ (Fig. 4a) remain close to a circular shape. In other words, the elastic interaction-induced pinning effect is slightly more prominent for larger dislocation loops.

To further demonstrate the size effect, we plot the evolution of the aspect ratio of the dislocation loops for an interloop spacing of $d = 32b$ in Fig. 5. The aspect ratio is defined as the ratio between the major and minor axes of the loop in Fig. 4 such that the major axis of the loop is always between the two screw-type dislocation segments. In other words, an aspect ratio greater than unity corresponds to the pinning of the edge segments, while an aspect ratio less than unity corresponds to negligible pinning effect. Until a critical amount of strain is reached, the circular loop will not grow, thus the aspect ratio remains at one initially. For a loop with an initial
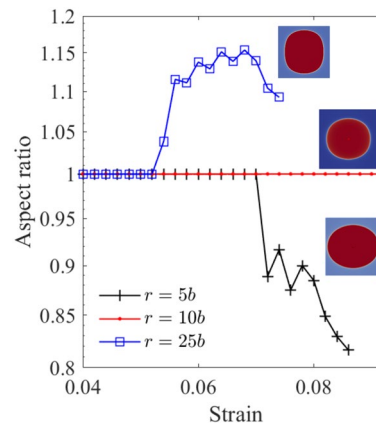


**Figure 5:** Evolution of the aspect ratio of a dislocation loop within an array over time under increasing applied strain with an initial radius of $r = 5b$, $10b$, or $25b$, and a loop spacing of $d = 32b$. The aspect ratio is defined as the major axis over the minor axis, where the major axis is taken as the spacing between the screw segments of the loop.

radius of $r = 5b$, the aspect ratio decreases to around 0.8 over time, and the initially circular loop becomes an oval-shaped one as shown in the inset of Fig. 5. As mentioned earlier in the discussion of Fig. 1, this is because the screw segments of the loop have lower self-energy, and thus it becomes energetically favorable for the loop to maximize these segments as it expands. For a larger initial loop size of $r = 10b$, the loop grows symmetrically, and the aspect ratio remains one over
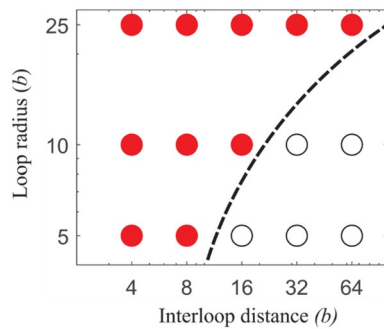
**Figure 6:** Diagram showing the transition of a strong pinning effect between dislocation loops to a weak/negligible pinning effect as a function of the loop radius and interloop spacing. A filled red circle indicates pinning of the edge segments was observed, and an open black circle indicates no-pinning effect was observed.



**Figure 7:** Evolution of the aspect ratio of a dislocation loop within an array with respect to strain at low (open symbols) and high (solid symbols) strain rates. Lower strain rate loading leads to longer edge segments. The loops have an initial radius of $r = 10b$ and the interloop spacing is $8b$ (red) and $32b$ (blue).

the entire deformation process. Finally, for the largest initial loop size of $r = 25b$, the aspect ratio keeps increasing once the dislocation loop starts to grow indicating that long edge-type dislocation segments are evolving as the loop grows. Evidently, the elastic interactions have a stronger effect on larger dislocation loops, leading to the higher aspect ratio for larger loops shown in Fig. 5.

Figure 6 presents a diagram that illustrates the transition of a strong pinning effect between dislocation loops to a weak/negligible pinning effect as a function of the interloop spacing and loop size. In particular, pinning of the edge segments is identified when the aspect ratio of the dislocation loop is greater than one. Our simulations show that the critical interloop spacing at which the elastic interaction-induced pinning effect dominates increases with increasing dislocation loop radius. This may be due to the fact that larger initial dislocation loops will also have longer pure edge and pure screw segments and, thus, the elastic interactions between longer initial pure edge segments would be expected to be stronger than the interactions between the relatively short pure edge segments in the smallest dislocation loops (i.e., $r = 5b$). This could cause a strong pinning effect in larger initial dislocation loops at larger interloop spacings as observed in our PFDD simulations.

## The effect of the strain rate

Finally, we study the strain rate effect by comparing loop growth at two different strain rates. In particular, we significantly decrease the strain rate (to $0.2 \dot{\varepsilon}$) with respect to simulations discussed in previous sections (which were run at $\dot{\varepsilon}$). Figure 7 shows the evolution of the loop aspect ratio at these two strain rates for a loop with an initial size of $r = 10b$ and for two interloop spacings of $d = 8b$ and $32b$. For an interloop spacing
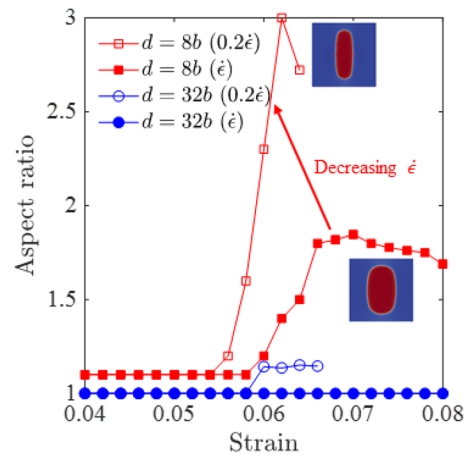
of $d = 32b$, the aspect ratio remains constant at one under high strain rate, while the aspect ratio slightly increases to a value larger than one under low strain rate loading. For the $d = 8b$ case, the aspect ratio is notably greater than one when loaded at a low strain rate, ending at an aspect ratio nearly twice what is achieved with the higher strain rate loading condition. Overall, the aspect ratio is in general higher at lower strain rates, i.e., the pinning effect becomes stronger at a lower strain rate. This can be understood from the competition between the homogeneous applied loading and the elastic interactions. Specifically, when the strain rate is lower, the elastic interactions dominate and result in the pinning of the edge segments. When the strain rate is higher, the homogeneous applied loading dominates and results in a weaker pinning effect between the edge-type dislocation segments.

Last but not least, it should be noted that the strain rate in PFDD simulations ($\sim 10^6$/s) is orders of magnitudes larger than experimental conditions ($10^{-3}$/s–$10^3$/s), and the dislocation loops simulated in this work are significantly smaller than those observed in experiments. Since our simulations revealed that slower strain rates and larger dislocation loop sizes are in favor of a stronger pinning effect on the edge segments, it can be expected that the elastic interaction-induced pinning effect under experimental conditions can result in loops with aspect ratios considerably higher than the aspect ratios predicted by the aforementioned simulations. We suspect that it is possible that the length of the edge segment could be one order of magnitude larger than the screw segment, resulting in the formation of dislocation walls that may impede subsequent dislocation motion. This might also contribute to the fact that extended edge dislocations are often observed in fcc metals [1, 2], which was

traditionally attributed to the easy cross slip and annihilation of the screw segments.

## Conclusions

In summary, we performed phase field dislocation dynamics (PFDD) simulations to study the evolution of an array of dislocation loops for various interloop spacings, loop sizes, and strain rates. We found that as the interloop spacing between glide planes decreases, the stress fields change significantly due to elastic interactions between dislocation loops on neighboring planes. At interloop spacings of $4b$ and $8b$ (and initial loop radius of $r = 5b$), edge-type dislocation segments experience a strong negative shear stress ($\sigma_{zx}$) that encourages loop collapse. Conversely, this stress surrounding the screw-type segments remains positive, encouraging loop expansion. This stress state results in anisotropic loop growth under homogeneous applied strain, where the screw-type segments move quickly creating a lens-shaped loop. This creates long, straight edge segments, which remain pinned in place, and relatively short screw segments. These long edge segment arrays could act as dislocation walls, impeding further dislocation motion.

Furthermore, the effect of the initial dislocation loop size and the applied strain rate on this pinning behavior was also investigated with PFDD. Interestingly, larger initial dislocation loop arrays exhibited the pinning of edge segments at larger interloop spacings. For the largest loop radius tested, $r = 25b$, the pinning effect was observed at all interloop spacings tested (ranging from 4 to $64b$). Lower strain rates were found to also enhance the pinning effect. Overall, elastic interactions, such as those observed in these PFDD simulation, could be an underlying formation mechanism for dislocation patterning and subgrain boundary formation.

## Methods

### Phase field dislocation dynamics

In PFDD, active phase field variables are defined over the entire simulation domain and represent the plastic slip in the unit of a perfect dislocation Burgers vector. Accordingly, any integer jump in the phase field variable indicates the location of a perfect dislocation.

The plastic strain ($\varepsilon_{ij}^p(r)$) is related to the phase field variables ($\xi(r)$) as [34]

$$\varepsilon_{ij}^p = \sum_{\alpha}^{N} \frac{1}{2} \xi^\alpha(\boldsymbol{r}) \left( b_i^\alpha m_j^\alpha + b_j^\alpha m_i^\alpha \right) \delta_\alpha \quad (2)$$

where $N$ is the number of active slip systems, $m^\alpha$ is the slip plane normal, $\boldsymbol{b}^\alpha$ is the Burgers vector, and $\delta_\alpha$ is a Dirac delta function that confines the slip on the slip plane, all for the slip system $\alpha$. In this work, we consider the dislocation interactions in one

active slip system ($N=1$) in Cu and, therefore, the normalized slip plane normal ($m$) and Burgers vector ($\boldsymbol{b}$) are $1/\sqrt{3}[1, 1, 1]$ and $1/2[1, 1, 0]$, respectively. The local strain can be calculated using the isotropic elastic Green's function, $G(r)$, as [34, 40, 51]

$$\varepsilon_{ij}(\boldsymbol{r}) = \overline{\varepsilon}_{ij} - C_{klmn}\varepsilon_{mn,l}^p(\boldsymbol{r}) * \frac{1}{2}\left( G_{ik,j}(\boldsymbol{r}) + G_{jk,i}(\boldsymbol{r}) \right) \quad (3)$$

where the "," in the subscript indicates partial derivative, $C_{klmn}$ is the elastic tensor, and "$*$" represents convolution. $\overline{\varepsilon}_{ij}$ is the homogeneous part of the strain and equals the applied strain $\varepsilon^{\text{applied}}$ under the strain-controlled loading condition adopted here. The local stress can be calculated as [51]

$$\sigma_{ij}(\boldsymbol{r}) = C_{ijkl}\left( \varepsilon_{kl}(\boldsymbol{r}) - \varepsilon_{kl}^p(\boldsymbol{r}) \right) \quad (4)$$

The evolution of the phase field variables is governed by energy minimization through a time-dependent Ginzburg–Landau equation [34],

$$\frac{\partial \xi^\alpha(\boldsymbol{r})}{\partial t} = -L \frac{\delta E}{\delta \xi^\alpha(\boldsymbol{r})} \quad (5)$$

where $L$ is the kinetic coefficient that determines dislocation velocity. The total energy ($E$) contains the elastic strain energy ($E_{\text{strain}}$) and the dislocation core energy ($E_{\text{core}}$). The former can be calculated as

$$\begin{aligned} E_{\text{strain}} &= \frac{1}{2} \int C_{ijkl}\left( \varepsilon_{ij}(\boldsymbol{r}) - \varepsilon_{ij}^p(\boldsymbol{r}) \right)\left( \varepsilon_{kl}(\boldsymbol{r}) - \varepsilon_{kl}^p(\boldsymbol{r}) \right) d^3r \\ &= \frac{V}{2} C_{ijkl}\overline{\varepsilon}_{ij}\overline{\varepsilon}_{kl} - C_{ijkl}\overline{\varepsilon}_{ij} \sum_\alpha \int \xi^\alpha(r)b_k^\alpha m_l^\alpha d^3r \\ &\quad + \frac{1}{2} \int \frac{d^3k}{(2\pi)^3} \hat{A}_{ijkl}(\boldsymbol{k}) \sum_{\alpha_1} \hat{\xi}^{\alpha_1}(k)b_i^{\alpha_1} m_j^{\alpha_1} \sum_{\alpha_2} \hat{\xi}^{\alpha_2*}(k)b_k^{\alpha_2} m_l^{\alpha_2} \end{aligned}$$
$$(6)$$

where $\hat{}$ denotes the Fourier transform, $k$ is the wave number vector in Fourier space, $*$ in the superscript indicates complex conjugate, and $\hat{A}_{ijkl}(\boldsymbol{k}) = C_{ijkl} - C_{ijuv}C_{mnkl}\hat{G}_{um}(\boldsymbol{k})k_v k_n$.

The core energy is calculated by integrating the planar energy density functional ($\Phi_n$) over the slip plane, $E_{\text{core}} = \int \Phi_n d^2r$. This energy density functional $\Phi_n$ is material dependent, and can even be slip system dependent and/or dependent on the dislocation type (i.e., edge, screw, or mixed) [44, 47]. Various functional forms have been used previously including piece wise quadratic [34], sinusoidal [48], tabular forms [52], and complex Fourier series [9, 39], and these forms are dependent on one or more phase field variables on a given slip plane. Here, our interest lies with fcc Cu and perfect dislocations from one active slip system. Therefore, a simple sinusoidal function [49, 53–55] is adopted, $\Phi_n = A \sin^2(\pi\xi)$, where the coefficient $A$ is the unstable stacking fault energy. Specifically, material parameters calculated with density functional theory are adopted, with an unstable stacking fault energy and shear
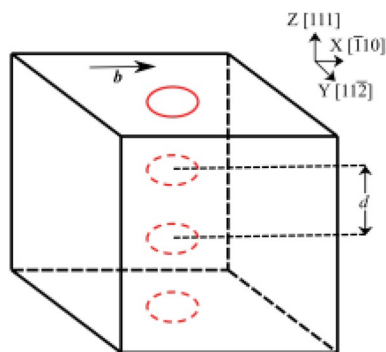
**Figure 8:** Schematic of the simulation setup with multiple dislocation loops initiated on parallel glide planes. *d* and b represent the interloop spacing and Burgers vector, respectively.

modulus of 163.7 mJ/m$^2$ [56] and 54.5 GPa, respectively, and the Poisson's ratio is 0.325.

### Simulation setup

As shown in Fig. 8, the initial dislocation array contains circular dislocation loops on parallel slip planes that are separated by an interloop spacing $d$. The dislocation loops belong to the same slip system with the Burgers vector $b$ along the $x$-axis and the slip plane normal along the $z$-axis. An increasing shear strain $\varepsilon_{zx}$ with the incremental step of $\Delta\varepsilon_{zx} = 0.002$, is applied to drive the dislocation loop growth. The simulation domain has a size of $128 \times 128 \times 128$ $b^3$, where $b$ is the grid size and corresponds to the Burgers vector magnitude of Cu, $b = 0.24$ nm. Periodic boundary conditions are applied in all three directions. A series of simulations are conducted for three initial loop radii ($5b$, $10b$, and $25b$) and multiple interloop spacing varying between 4 and $64b$. Two different strain rates are adopted in "The effect of the strain rate" section. In particular, following each strain increment, the structure is allowed to relax for five times longer in the low strain rate case than the high strain rate case, which qualitatively represents the strain rate effect.

### Acknowledgments

### Authors contributions

PC conducted the simulations and processed the data under the supervision of LC. All authors discussed the data and wrote the manuscript.

### Funding

### Data Availability

Requests for materials and data should be addressed to the corresponding authors.

### Code availability

Custom code.

### Declarations

**Conflict of interest** On behalf of all authors, the corresponding authors state that there is no conflict of interest.

### References

1. H. Mughrabi, Dislocation wall and cell structures and long-range internal stresses in deformed metal crystals. Acta Metall. **31**(9), 1367–1379 (1983)

2. D. An, S. Zaefferer, Formation mechanism of dislocation patterns under low cycle fatigue of a high-manganese austenitic trip steel with dominating planar slip mode. Int. J. Plast **121**, 244–260 (2019)

3. Y. Kawasaki, T. Takeuchi, Cell structures in copper single crystals deformed in the [001] and [111] axes. Scr. Metall. **14**(2), 183–188 (1980)

4. G. Zhang, R. Schwaiger, C. Volkert, O. Kraft, Effect of film thickness and grain size on fatigue-induced dislocation structures in cu thin films. Philos. Mag. Lett. **83**(8), 477–483 (2003)

5. D. Hughes, N. Hansen, The microstructural origin of work hardening stages. Acta Mater. **148**, 374–383 (2018)

6. N. Grilli, K.G. Janssens, J. Nellessen, S. Sandlobes, D. Raabe, Multiple slip dislo cation patterning in a dislocation-based crystal plasticity finite element method. Int. J. Plast. **100**, 104–121 (2018)

7. G.I. Taylor, The mechanism of plastic deformation of crystals. Part I—theoretical. Proc. R. Soc. Lond Ser. A **145**(855), 362–387 (1934)

8. K. Hattar, Deformation structures including twins in nanograined pure metals. in *Nanos tructured Metals and Alloys* (Elsevier, 2011), pp. 213–242

9. S. Zheng, D. Zheng, Y. Ni, L. He, Improved phase field model of dislocation inter sections. npj Comput. Mater. **4**(1), 1–8 (2018)

10. A.H. Zahiri, P. Chakraborty, Y. Wang, L. Cao, Strong strain hardening in ultrafast melt-quenched nanocrystalline cu: the role of fivefold twins. J. Appl. Phys. **126**(7), 075103 (2019)

11. A.H. Cottrell, *Dislocations and Plastic Flow in Crystals*, 1953

12. M. Duesbery, *Dislocations in Solids*. North Holland, 2002

13. L. Kubin, B. Devincre, T. Hoc, The deformation stage II of face-centered cubic crystals: fifty years of investigations. Int. J. Mater. Res. **100**(10), 1411–1419 (2009)

14. L. Laurson, J. Rosti, J. Koivisto, A. Miksic, M.J. Alava, Spatial fluctuations in transient creep deformation. J. Stat. Mech: Theory Exp. **2011**(07), P07002 (2011)

15. N. Koneva, D. Lychagin, L. Trishkina, E. Kozlov, Types of dislocation substructures and stages of stress-strain curves of fcc alloys, in *Strength of Metals and Alloys (ICSMA 7)* (Elsevier, 1985), pp. 21–26

16. J. Boutin, J. Dickson, J.-P. Baïlon, The cyclic deformation of 70–30 α-brass: internal and effective stresses and dislocation substructures, in *Time-Dependent Fracture*, (Springer, 1985), pp. 13–26

17. L. Kubin, *Materials Science and Technology: Plastic Deformation and Fracture of Materials*, vol 6 mughrabi (1996)

18. C. Depres, C. Robertson, M. Fivel, Low-strain fatigue in aisi 316l steel surface grains: a three-dimensional discrete dislocation dynamics modelling of the early cycles I. Dislocation microstructures and mechanical behavior. Philos. Mag. **84**(22), 2257–2275 (2004)

19. R. Madec, B. Devincre, L. Kubin, Simulation of dislocation patterns in multislip. Scripta Mater. **47**(10), 689–695 (2002)

20. M. Shehadeh, H. Zbib, T. De La Diaz Rubia, Modelling the dynamic deformation and patterning in fcc single crystals at high strain rates: dislocation dynamics plasticity analysis. Philos. Mag. **85**(15), 1667–1685 (2005)

21. O. Dmitrieva, J. Svirina, E. Demir, D. Raabe, Investigation of the internal sub structure of microbands in a deformed copper single crystal: experiments and dislocation dynamics simulation. Modell. Simul. Mater. Sci. Eng. **18**(8), 085011 (2010)

22. D. Raabe, F. Roters, G. Gottstein, Simulation of the statics of 2d and 3d dislocation networks. Comput. Mater. Sci. **5**(1–3), 203–209 (1996)

23. B. Devincre, T. Hoc, L. Kubin, Dislocation mean free paths and strain hardening of crystals. Science **320**(5884), 1745–1748 (2008)

24. L. Kubin, B. Devincre, T. Hoc, Toward a physical model for strain hardening in fcc crystals. Mater. Sci. Eng., A **483**, 19–24 (2008)

25. Z. Wang, I. Beyerlein, R. LeSar, The importance of cross-slip in high-rate deformation. Modell. Simul. Mater. Sci. Eng. **15**(6), 675 (2007)

26. Y. Cui, G. Po, N. Ghoniem, Size-tuned plastic flow localization in irradiated materials at the submicron scale. Phys. Rev. Lett. **120**(21), 215501 (2018)

27. Y. Cui, G. Po, P. Srivastava, K. Jiang, V. Gupta, N. Ghoniem, The role of slow screw dislocations in controlling fast strain avalanche dynamics in body-centered cubic metals. Int. J. Plast **124**, 117–132 (2020)

28. S. Xia, A. El-Azab, Computational modelling of mesoscale dislocation patterning and plastic deformation of single crystals. Modell. Simul. Mater. Sci. Eng. **23**(5), 055009 (2015)

29. C. Zhou, C. Reichhardt, C.J.O. Reichhardt, I.J. Beyerlein, Dynamic phases, pinning and pattern formation for driven dislocation assemblies. Sci. Rep. **5**(1), 1–7 (2015)

30. S. Sandfeld, M. Zaiser, Pattern formation in a minimal model of continuum dislocation plasticity. Modell. Simul. Mater. Sci. Eng. **23**(6), 065005 (2015)

31. R. Wei, A. Baker, Observation of dislocation loop arrays in fatigued polycrystalline pure iron. Philos. Mag. **11**(113), 1087–1091 (1965)

32. Y. Cui, G. Po, N. Ghoniem, Does irradiation enhance or inhibit strain bursts at the submicron scale? Acta Mater. **132**, 285–297 (2017)

33. Y.S. Chen, W. Choi, S. Papanikolaou, M. Bierbaum, J.P. Sethna, Scaling theory of continuum dislocation dynamics in three dimensions: self-organized fractal pattern formation. Int. J. Plast **46**, 94–129 (2013)

34. M. Koslowski, A.M. Cuitino, M. Ortiz, A phase-field theory of dislocation dynamics, strain hardening and hysteresis in ductile single crystals. J. Mech. Phys. Solids **50**(12), 2597–2635 (2002)

35. G. Schoeck, The core structure, recombination energy and peierls energy for dislocations in Al. Philos. Mag. A **81**(5), 1161–1176 (2001)

36. V. Vitek, M. Mrovec, J. Bassani, Influence of non-glide stresses on plastic flow: from atomistic to continuum modeling. Mater. Sci. Eng. A **365**(1–2), 31–37 (2004)

37. L. Cao, M. Koslowski, Effect of microstructural uncertainty on the yield stress of nanocrystalline nickel. Acta Mater. **61**(4), 1413–1420 (2013)

38. L. Cao, A. Sengupta, D. Pantuso, M. Koslowski, Effect of texture and grain size on the residual stress of nanocrystalline thin films. Modell. Simul. Mater. Sci. Eng. **25**(7), 075004 (2017)

39. A. Hunter, R. Zhang, I. Beyerlein, T.C. Germann, M. Koslowski, Dependence of equilibrium stacking fault width in fcc metals on the γ-surface. Modell. Simul. Mater. Sci. Eng. **21**(2), 025015 (2013)

40. L. Cao, A. Hunter, I.J. Beyerlein, M. Koslowski, The role of partial mediated slip during quasi-static deformation of 3d nanocrystalline metals. J. Mech. Phys. Solids **78**, 415–426 (2015)

41. L. Cao, M. Koslowski, Rate-limited plastic deformation in nanocrystalline Ni. J. Appl. Phys. **117**(24), 244301 (2015)

42. Y. Zeng, A. Hunter, I.J. Beyerlein, M. Koslowski, A phase field dislocation dynamics model for a bicrystal interface system: an

investigation into dislocation slip transmission across cube-on-cube interfaces. Int. J. Plast **79**, 293–313 (2016)

43. H. Mori, H. Kimizuka, S. Ogata, Microscopic phase-field modeling of edge and screw dislocation core structures and peierls stresses of bcc iron. J. Jpn. Inst. Met. **75**(2), 104–109 (2011)

44. X. Peng, N. Mathew, I.J. Beyerlein, K. Dayal, A. Hunter, A 3d phase field dislocation dynamics model for body-centered cubic crystals. Comput. Mater. Sci. **171**, 109217 (2020)

45. D. Qiu, P. Zhao, C. Shen, W. Lu, D. Zhang, M. Mrovec, Y. Wang, Predicting grain boundary structure and energy in bcc metals by integrated atomistic and phase-field modeling. Acta Mater. **164**, 799–809 (2019)

46. Y. Zeng, X. Cai, M. Koslowski, Effects of the stacking fault energy fluctuations on the strengthening of alloys. Acta Mater. **164**, 1–11 (2019)

47. C. Albrecht, A. Hunter, A. Kumar, I.J. Beyerlein, A phase field model for disloca tions in hexagonal close packed crystals. J. Mech. Phys. Solids **137**, 103823 (2020)

48. I. Beyerlein, A. Hunter, Understanding dislocation mechanics at the mesoscale using phase field dislocation dynamics. Philos. Trans. R. Soc. A **374**(2066), 20150166 (2016)

49. J.P. Hirth, J. Lothe, Theory of dislocations. J. Appl. Mech. **50**(2), 476 (1983)

50. N. Langdon, Explicit expressions for stress field of a circular dislocation loop. Theoret. Appl. Fract. Mech. **33**(3), 219–231 (2000)

51. T. Mura, *Micromechanics of Defects in Solids* (Springer, New York, 2013)

52. S. Xu, J.R. Mianroodi, A. Hunter, I.J. Beyerlein, B. Svendsen, Phase-field-based calculations of the disregistry fields of static extended dislocations in fcc metals. Philos. Mag. **99**(11), 1400–1428 (2019)

53. Y. Zhu, X. Liao, S. Srinivasan, E. Lavernia, Nucleation of deformation twins in nanocrystalline face-centered-cubic metals processed by severe plastic deformation. J. Appl. Phys. **98**(3), 034319 (2005)

54. J. Douin, F. Pettinari-Sturmel, A. Coujou, Dissociated dislocations in confined plasticity. Acta Mater. **55**(19), 6453–6458 (2007)

55. E. Martinez, J. Marian, A. Arsenlis, M. Victoria, J. Perlado, Atomistically informed dislocation dynamics in fcc crystals. J. Mech. Phys. Solids **56**(3), 869–895 (2008)

56. A. Hunter, R. Zhang, I. Beyerlein, The core structure of dislocations and their relationship to the material γ-surface. J. Appl. Phys. **115**(13), 134314 (2014)